

Flow Control Using Synthetic Jet and Plasma Actuators on a Rotorcraft Tail Boom Model

Sarah J. Haack*

Johns Hopkins University Applied Physics Laboratory, Laurel, MD, 20723, USA

Alison B. Flatau†

University of Maryland, College Park, MD, 20742, USA

Abstract

This paper shows the time-averaged effect of synthetic jet and plasma actuators on flow over a representative two-dimensional rotorcraft tail boom for delaying flow separation and, therefore, reducing pressure drag, whereas previous studies have evaluated these flow control devices on a circular cylinder. The percentage of pressure drag reduction is used to evaluate the effectiveness of these two unique actuators for varied applied voltage under device independent conditions such as actuator position and flow velocity. Two non-dimensional parameters were used to evaluate the effect of the actuators: coefficient of momentum (C_μ) and non-dimensional surface distance between the location of the actuator and the flow separation point (SD_{TB}). Both actuation techniques beneficially affect the pressure distribution by decreasing the pressure near the location of the actuators and increasing the pressure in the separated flow region. Contour plots displaying the variation of the percentage of pressure drag reduction as C_μ and SD_{TB} vary illustrate optimal operating conditions based on these parameters. While this study is not a one-to-one comparison of these two devices, the results clearly show that, under the same external flow conditions, synthetic jet actuators have a global effect where as plasma actuators have a local effect both reducing the pressure drag up to 40% and 45%, respectively.

NOMENCLATURE

b	Orifice width
c	Tail boom chord length
C	coefficient
l	Length
r	Radius
P	Pressure
SD	Non-dimensional Surface Distance
x	Distance from the leading edge
θ	Angular location
ρ	Density

Subscript

a	Actuator
D	Drag
f	Front
j	Jet value
p	Pressure
s	Flow Separation point
S	Static value
ta	Tail boom actuator

*Aerospace Engineer, Global Engagement Department, 11100 Johns Hopkins Road, Mailstop 24-W430, and AIAA Member.

†Professor, Department of Aerospace Engineering, 3184 Glenn L. Martin Hall, and AIAA Senior Member.

TB	Tail boom
t_s	Tail boom flow separation point
∞	Freestream value
μ	Momentum

1. INTRODUCTION

Significant pressure drag is usually associated with bluff bodies due to flow separation over a large region of the surface. In the case of a rotorcraft tail boom, the induced flow from the main rotor flows over the top of the tail boom and then separates over the bottom portion of the tail boom resulting in a net downward force. This download affects helicopter performance characteristics such as payload capability, range and maneuverability. Other research^{1,2} conducted at NASA Langley Research Center suggests that separated flow actually improves overall rotorcraft performance by off-loading the tail rotor allowing more power for the main rotor. The benefits of the additional power to the main rotor outweighs the reduction in download force by maintaining attached flow. While this work uses active flow control to reduce the download force, the devices could be arranged in a number of ways to affect the pressure distribution and possibly further alleviate the side force on the tail boom. Understanding what causes the flow to separate from the surface helps provide insight for understanding how AFC devices work to delay flow separation. A circular cylinder is a common platform for studying bluff body flow because it has been well characterized and modeled through many experimental and theoretical studies for over a century.³ Many of the flow phenomenon associated with a circular cylinder, such as significant flow separation and pressure drag, are observed on the tail boom shape as well. In ideal conditions, air flow is assumed to be inviscid and incompressible such that, when considering flow over bluff body shapes symmetric about the direction of the oncoming flow, there is no flow separation and, therefore, no net lift, drag or moment. The corresponding ideal pressure distribution for a circular cylinder is given in terms of the non-dimensional pressure coefficient C_p by either form of Equation 1:

$$C_p(\theta) = 1 - 4 \sin^2(\theta) = \frac{P_s(\theta) - P_\infty}{\frac{1}{2} \rho_\infty U_\infty^2} \quad (1)$$

where $\theta = 0^\circ$ is the angular position on the cylinder surface facing the incoming free stream flow, P_s is the static pressure on the cylinder surface and P_∞ , ρ_∞ and U_∞ are the static pressure, air density and freestream velocity of the external flow, respectfully. The second portion of the equation can be applied to any shape where P_s changes according to the surface location of the static pressure measurement. In typical flow conditions, however, viscous forces are present and result in the thickening of the boundary layer, flow separation and pressure drag. A paper by Achenbach⁴ presents a high resolution progression of the shear stress and pressure distribution around a cylinder indicating that flow separation corresponds to the region of nearly constant pressure over the rear half of the cylinder. The corresponding pressure drag coefficient (C_D) is found by integrating the components of the pressure coefficient parallel to the flow direction over the entire pressure distribution around the circular cylinder as shown in Equation 2.

$$C_D = \int_0^{2\pi} C_p(\theta) \cos(\theta) d\theta \quad (2)$$

For a viscous flow pressure distribution, C_D is greater than zero due, in large part, to flow separation and the resulting imbalance of the pressure forces around the bluff body shape. Because the tail boom shape is not circular, the magnitude of the downstream components of the pressure coefficient is based on the slope of the tail boom surface. The drag distribution was summed, using the Trapezoidal Rule, to calculate C_D . In this paper, the effectiveness of the AFC devices is evaluated by calculating the percentage of pressure drag reduction from the baseline case, with actuators installed but not operating, to the actuator on case.

While there is extensive research on bluff body flow, plasma actuators and synthetic jet actuators, there is relatively little research involving a combination of either of these two active flow control devices on bluff bodies. Synthetic jet actuators have been used on circular cylinders to delay flow separation^{5, 6} and plasma actuators have been used primarily for control of the vortex shedding frequency.^{7, 8} To the author's knowledge, this paper reports the only source of research using both types of AFC devices on a tail boom model. Significant contributions from this research include the pressure

distribution over the tail boom shape and, in addition, the use of synthetic jet and plasma actuators in identical flow conditions on this shape.

1.2 Active Flow Control Devices

Flow separation is a boundary layer phenomenon that affects the lift and drag characteristics of flow over aerodynamic surfaces. To avoid adverse effects, flow control devices have been used on aircraft to delay flow separation. There are two main categories of flow control devices: passive and active. Passive devices are fixed alterations on the surface of a body in a flow. While these devices improve flow characteristics, they are point-design devices; therefore, when the aircraft is in off-design flight conditions, the devices are still on the surface in the external flow and may induce adverse effects. A more recent development in the engineering research community is active flow control devices. These devices have the unique ability to operate only when needed to improve flow characteristics. In supersonic flows, unsteady actuation operating at a frequency $O(10^3)$ and higher is required. One targeted application requiring high frequency actuation is noise suppression of jet impingement tones that can occur in open cavity flows such as exposed landing gear or cargo bays. Glow discharge plasma,⁹ steady microjets¹⁰ and powered resonance tubes¹¹ are AFC devices that have demonstrated the ability to attenuate the tones specifically associated with jet impingement. For low speed flows, low frequency actuators are required to match the natural unsteadiness in the external flow. Two examples of AFC devices used for low frequency unsteady actuation are discussed further in this paper: synthetic jet and plasma actuators.

1.2.1 Synthetic Jet Actuators

A synthetic jet actuator (SJA) is a zero-net-mass-flux (ZNMF) device consisting of a closed cavity with a small orifice from the cavity to the external flow. The pressure inside the cavity is controlled, typically using a flexing diaphragm, such that when the pressure decreases, low momentum air from the boundary layer is drawn into the cavity through the orifice. When the cavity pressure increases, the air is reenergized and ejected into the external flow through the orifice forming a synthetic jet. With the appropriate combination of geometric and operating parameters, vortices form as the air passes the edges of the orifice as shown in Figure 1. In a cross flow, the vortices move downstream and result in an addition of momentum to the boundary layer. Glezer¹² provides a comprehensive review of SJAs and their applications.

The design for the synthetic jets used for this research was provided by The Boeing Company in Seattle, WA. The actuators were positioned to energize the boundary layer through 152 mm x 2.5 mm spanwise slots such that the SJAs ejected air perpendicular to the surface of the tail boom. The actuators were capable of producing velocities of up to 9 m/s when excited at their fundamental frequency which varied from 95 - 105 Hz depending on small variations in the actuator construction.

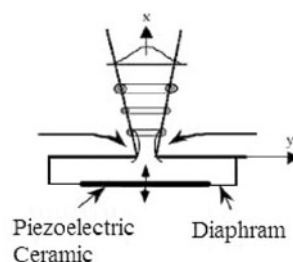


Figure 1. Flow concept for a synthetic jet.¹²

1.2.2. Plasma Actuators

A plasma actuator consists of two electrodes, an exposed and insulated electrode, separated by a dielectric and offset from each other (asymmetric configuration) as shown in Figure 2. A high voltage (1-20 kV_{p-p}), high frequency (3-20 kHz) AC signal is applied across the electrodes. This configuration and the very high applied voltage level produce a dielectric barrier discharge (DBD) plasma on the dielectric covering the insulated electrode. During the forward stroke, the applied voltage is positive-going and the air density above the insulated electrode increases effectively trapping a pocket of air. During the backward stroke, the applied voltage is negative-going and the pocket of air is released

downstream.¹³ This stroke sequence repeats at the frequency of actuation and creates an induced flow tangential to the surface from the exposed electrode toward the insulated electrode.

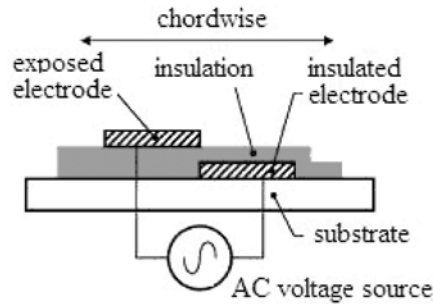


Figure 2. Plasma actuator setup.¹⁴

The materials used for the plasma actuator construction were two 152 mm-long x 6.35 mm-wide strips of 0.06 mm-thick copper tape and one 152 mm-long x 19 mm wide strip of 0.12 mm-thick Kapton tape. The upper electrode was wired to ground while the lower electrode was wired to the high voltage signal. The resulting induced flow was downstream and tangential to the surface.

1.2.3 Non-dimensional Parameters

A commonly used non-dimensional parameter to indicate the ratio of the device to freestream momentum flux is the coefficient of momentum (C_μ), given in Equation 3, where ρ_j and U_j are the density and velocity of the jet fluid, b is the orifice width and c is the tail boom chord length. The value of C_μ is typically orders of magnitude less than 1.

$$C_\mu = \frac{2\rho_j U_j^2 b}{\rho U_\infty^2 c} \quad (3)$$

Based on the pressure drag reduction results in the test matrix, one consideration addressed is that the changing Reynolds number (Re), the ratio of inertial to viscous forces of the external flow, affected the location of the flow separation point. The approach taken to normalize results associated with different separation and actuator angle locations was to identify a non-dimensional surface distance parameter; SD . SD is the surface distance between the flow separation point and the actuator location ($\theta_{ts} - \theta_{ta}$) normalized by the surface distance from the leading edge of the tail boom ($\frac{180}{\pi r} l_f + \theta_{ts}$) where l_f is the surface distance over the front portion of the tail boom cross-section) to the flow separation point.

$$SD_{TB} = \frac{\theta_{ts} - \theta_{ta}}{\frac{180}{\pi r} l_f + \theta_{ts}} \quad (4)$$

These two parameters, C_μ and SD_{TB} (TB subscript for *tail boom*), are used in the results to identify optimal parameters for operating and placing the actuators.

2. EXPERIMENTAL SETUP

The wind tunnel facility used for the test was the NASA Langley Research Center 0.51m x 0.71m shear flow wind tunnel. It is a low speed, open circuit facility with a maximum speed of 45 m/s. Wind tunnel and room atmospheric conditions were recorded before each test including temperature, relative humidity, barometric pressure, wind tunnel entrance velocity and velocity profile at the position in the tunnel where the model was located. The tail boom model, constructed using Stereolithography Apparatus (SLA), had a 152 mm chord length and spanned the entire height of the wind tunnel test section. There were 58 pressure ports on the tail boom spaced such that they were more concentrated where flow separation was expected to provide high resolution pressure distribution measurements in that area. Figure 3 shows the pressure port locations around the tail boom and the model itself with the plasma actuators installed.

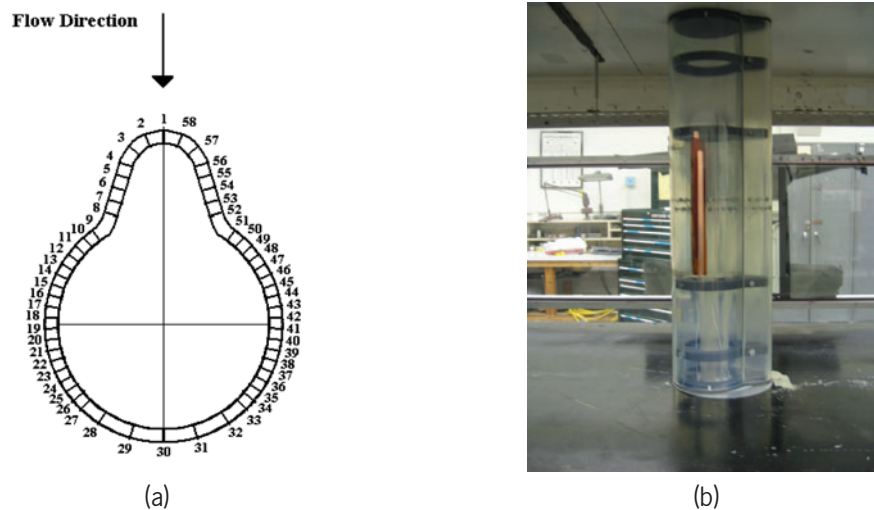


Figure 3. Tail boom model a) pressure port distribution and locations and b) wind tunnel model with plasma actuators installed.

To operate the actuators, unique electronic setups were required based on the voltage requirements of each actuator. A maximum voltage of $1000 V_{p-p}$ at 5 mA was used to operate the SJAs using a waveform generator and voltage amplifier. The applied voltage was varied from 200 to $1000 V_{p-p}$ at increments of $200 V_{p-p}$. The electronic setup for the plasma actuator includes a signal generator, intermediate amplifier and a step up transformer to meet the high voltage requirements for operation. The actuators were operated using an AC sine wave with a frequency of 5 kHz and applied voltage varied at increments of $1.4V_{p-p}$ from $2.8 V_{p-p}$ to $11.8 kV_{p-p}$. For both actuator setups, the applied voltage and current drawn from the actuators was read and recorded using a LeCroy 9100 Series Oscilloscope.

The test matrix for this research was designed to observe the effectiveness of the plasma and synthetic jet actuators as Re, angular position of the actuators and applied voltage were each varied. Three freestream velocities were used, corresponding to laminar flow conditions at Reynolds numbers of 2.48×10^4 , 4.8×10^4 and 7.3×10^4 and flow separation positions of $(x/c)_s = 0.67$, 0.67 and 0.74 , respectively. The five angular positions of the actuators varied from $(x/c)_a = 0.43$ to 0.71 .

Note that while this study considers similar operating and external flow conditions, the two devices used in this testing operated using different mechanisms. The synthetic jet actuators injected flow normal to the surface of the cylinder while the plasma actuators caused forcing on the flow tangent to the surface. Also, to match the flow velocity produced by the synthetic jet actuators by the plasma actuators required a higher applied voltage than could be sustained by this particular plasma actuator design and, therefore, was not matched. Future work would involve improving the plasma actuator design such that higher velocities could be obtained and the synthetic jet orifice would be shaped such that the induced flow acts tangent to the surface.

3. RESULTS

For this research, active flow control actuators were being used to reduce pressure drag by changing the time-averaged pressure distribution such that it approached the inviscid theoretical pressure distribution solution. The arrows in Figure 4 show the directions needed for favorable changes in pressure profiles obtained for flow over the tail boom model with no flow control for laminar flow conditions. Also, the location of the onset of flow separation, which is evident from the pressure distribution as the location at which a plateau in the pressure profile first occurs, is expected to shift downstream. For this paper, the variations in the pressure distribution and pressure drag due to the changing freestream velocity are not included because the conclusions are relatively insignificant. However, the results are presented and discussed extensively elsewhere.¹⁵

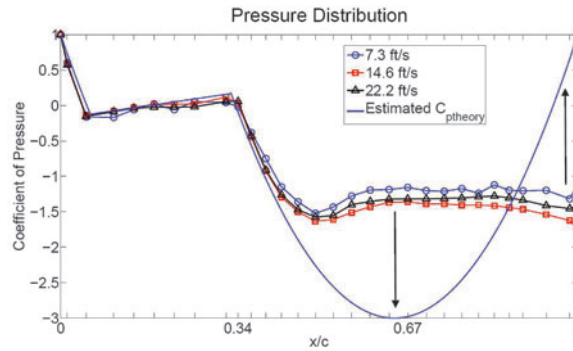


Figure 4. The black arrows show the desired trends in the pressure distribution for delaying flow separation and reducing pressure drag for 7.3, 14.6 and 22.2 ft/s ($Re = 2.4 \times 10^4$, 4.8×10^4 and 7.3×10^4).

3.1 Synthetic Jet Actuator Data

To illustrate the effect of the synthetic jet actuators on the tail boom pressure distribution, Figure 5 shows the change in the pressure distribution when the actuators are placed at $x/c = 0.56$, actuated using $1000 V_{p-p}$ and $Re = 7.3 \times 10^4$ ($U_\infty = 22.2$ ft/s). The actuator off pressure distribution is represented by the black circles and the actuator on pressure distribution is represented by the red squares. The hollow points represent interpolated data to show an approximation of the pressure distribution over the blocked pressure ports. The magenta band shows the location of the actuators. The SJAs cause the pressure distribution near the actuator location to decrease slightly, although this is based on interpolation points and the actual effect may be more or less. The actuators also cause the pressure in the separated flow region ($x/c = 1.0$) to increase which leads to a reduction in pressure drag.

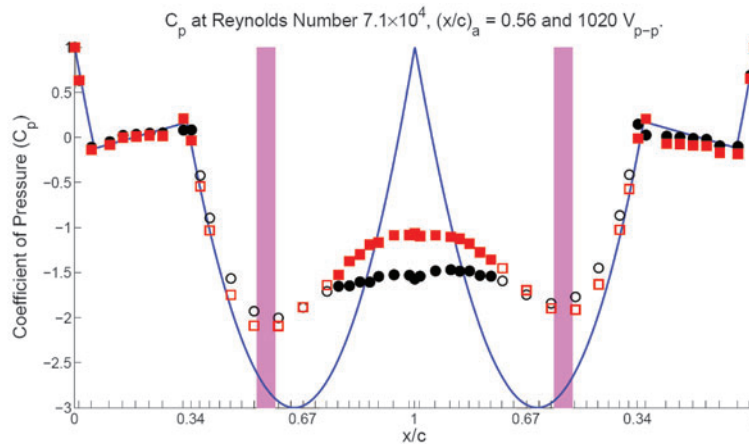
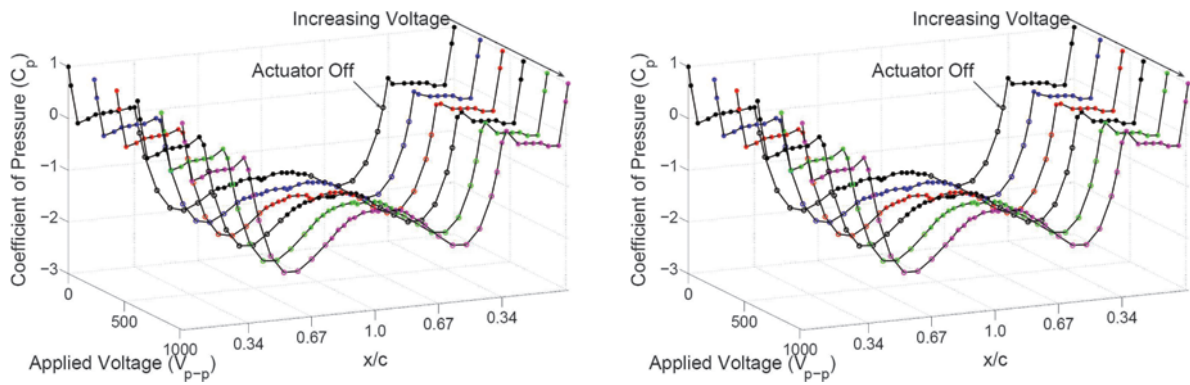


Figure 5. Pressure distribution showing the effect of two synthetic jet actuators on the tail boom pressure distribution when placed at $(x/c)_a = 0.56$ with an applied voltage of $1000 V_{p-p}$ and $Re = 7.3 \times 10^4$. ($U_\infty = 22.2$ ft/s, $(x/c)_s = 0.74$, $SD_{TB} = 0.11$)

3.1.1 Variation with Applied Voltage

Figure 6b shows the variation in the pressure distribution around the tail boom as the applied voltage increases from $200 V_{p-p}$ to $1000 V_{p-p}$ at increments of $200 V_{p-p}$. The actuators are located at $x/c = 0.56$ and $Re = 7.3 \times 10^4$ ($U_\infty = 22.2$ ft/s, $(x/c)_s = 0.74$, $SD_{TB} = 0.11$). At the lowest applied voltage, the pressure distribution resembles the baseline pressure distribution. As the voltage increases, the pressure drops very slightly at the location of the actuators and the pressure in the separated flow region increases.

The corresponding percentage of pressure drag reduction for the pressure distributions in Figure 6b is shown in Figure 6a. As the voltage increases, the percentage of pressure drag reduction increases gradually at first (up to $V = 400 V_{p-p}$) and then more quickly. Beyond $V = 600 V_{p-p}$, the increasing pressure drag reduction starts to show evidence of a maximum percentage of pressure drag reduction but is not achieved within the voltages tested.

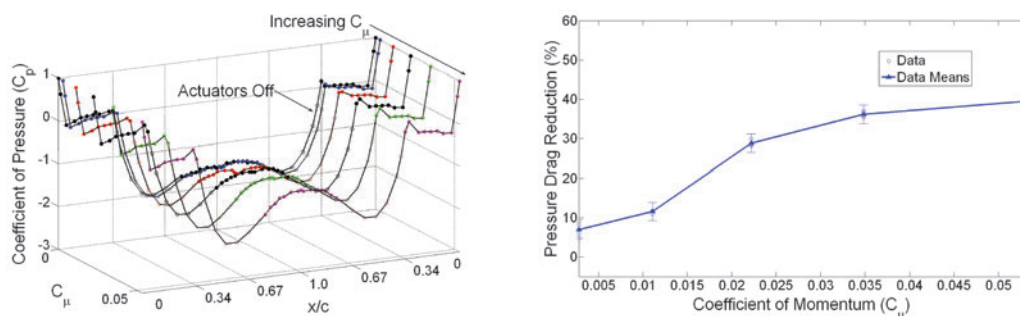


(a) Waterfall plot of the variation in the pressure distribution.

(b) Percentage of pressure drag reduction.

Figure 6. Variation as the applied voltage increases from 200 V_{p-p} to 1000 V_{p-p} ($Re = 7.3 \times 10^4$, $U_\infty = 22.2$ ft/s, $(x/c)_s = 0.74$, $(x/c)_a = 0.56$, $SD_{TB} = 0.11$)

Increasing the applied voltage is similar to increasing the coefficient of momentum (C_μ). Figure 7a shows the same pressure distribution data shown in Figure 6b plotted using C_μ instead of voltage. This shows that large changes in the pressure distribution occur over a small range of low C_μ values, i.e. C_μ less than 0.022, beyond which, there is little change in the pressure distribution despite large changes in C_μ . This observation is also evident in Figure 7b where there is a rapid increase in the pressure drag reduction up to $C_\mu = 0.022$ after which there is a gradual increase that approaches a local maximum up to $C_\mu = 0.053$.



(a) Waterfall plot of the variation in the pressure distribution.

(b) Percentage of pressure drag reduction.

Figure 7. Variation as the coefficient of momentum increases from 0.003 to 0.053. ($Re = 7.3 \times 10^4$, $U_\infty = 22.2$ ft/s, $(x/c)_s = 0.74$, $(x/c)_a = 0.56$, $SD_{TB} = 0.11$)

3.1.2 Variation with Actuator Position

Figure 8a shows the change in the pressure distribution as the actuator location moves downstream from $(x/c)_a = 0.43$ to 0.71 by two-port increments (equivalent to 11° on the larger diameter part of the model). The applied voltage is 1000 V_{p-p} ($C_\mu = 0.053$) and $Re = 7.3 \times 10^4$ ($U_\infty = 22.2$ ft/s, $(x/c)_s = 0.74$). The pressure near the location of the actuators generally decreases until $(x/c)_a = 0.54$ and then increases at $(x/c)_a = 0.71$. The pressure in the separated flow region increases from $(x/c)_a = 0.43$ to 0.49. Between $(x/c)_a = 0.49$ and 0.54, the pressure remains fairly constant and then decreases at $(x/c)_a = 0.71$.

Figure 8b shows the effect of moving the actuators downstream on the percentage of pressure drag reduction. Pressure drag reduction increases up to $(x/c)_a = 0.54$ and then decreases as $(x/c)_a$ continues to increase. The percentage of pressure drag reduction is also shown with an SD_{TB} on the top axis. This plot shows that the actuators are most effective at $SD_{TB} = 0.17$.

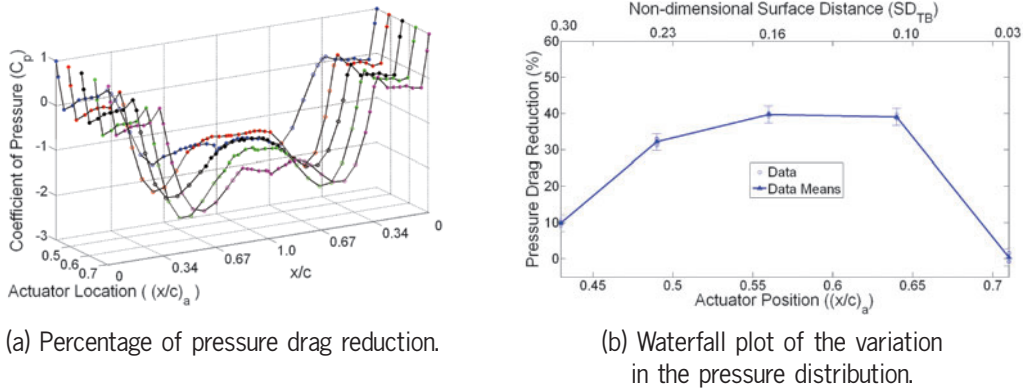


Figure 8. Variation as the actuator position moves downstream from $(x/c)_a = 0.43$ to 0.71 . ($Re = 7.3 \times 10^4$, $U_\infty = 22.2$ ft/s, $(x/c)_s = 0.74$, $V = 1000$ V_{p-p} , $C_\mu = 0.053$)

3.1.3 SD_{TB} vs C_μ

As discussed in the previous sections, two factors influence the effectiveness of the actuators for reducing pressure drag: the momentum coefficient (C_μ) and the distance between the flow separation point and the actuator position (SD_{TB}). The following contour plots show the effect of both parameters on the percentage of pressure drag reduction for each velocity. The black points on the contour plot represent the actual SD_{TB} and C_μ values for which the percentages of pressure drag reduction were taken.

Figure 9a shows the variation in pressure drag reduction with SD_{TB} and C_μ for $Re = 2.4 \times 10^4$ ($U_\infty = 7.3$ ft/s). For constant C_μ , the percentage of pressure drag reduction increases as SD_{TB} increases to 0.18, beyond which pressure drag reduction decreases rapidly. For constant SD_{TB} , the percentage of pressure drag reduction is relatively constant as C_μ increases except at $SD_{TB} = 0.18$ where pressure drag reduction steadily increases. This contour plot clearly shows that the actuators are most effective at $SD_{TB} = 0.18$ for C_μ values above 0.2.

Figure 9b shows the variation in pressure drag reduction with SD_{TB} and C_μ for $Re = 4.8 \times 10^4$ ($U_\infty = 14.6$ ft/s). For constant C_μ , the percentage of pressure drag reduction increases as SD_{TB} increases to 0.18 beyond which pressure drag reduction decreases rapidly (same as Figure 9a). For constant SD_{TB} , the percentage of pressure drag reduction is relatively constant as C_μ increases above $C_\mu = 0.3$. This contour plot clearly shows, again, that the actuators are most effective at $SD_{TB} = 0.18$ for C_μ values above 0.3.

Figure 9c shows the variation in pressure drag reduction with SD_{TB} and C_μ for $Re = 7.3 \times 10^4$ ($U_\infty = 22.2$ ft/s). For constant C_μ , the percentage of pressure drag reduction increases as SD_{TB} increases to 0.10 beyond which pressure drag reduction is relatively constant up to $SD_{TB} = 0.25$ and then decreases gradually. For constant SD_{TB} , the percentage of pressure drag reduction increases as C_μ increases except for SD_{TB} less than 0.1 and greater than 0.25. This contour plot shows that the actuators are most effective between $SD_{TB} = 0.1$ and 0.25 for C_μ values above 0.2.

Based on all three contour plots (Figures 9a - 9c), the range of SD_{TB} values for which the actuators are most effective centers around $SD_{TB} = 0.18$ but this range expands as velocity increases. This could be due to increased instability in the laminar flow as velocity increases and, therefore, the actuators can influence the boundary layer over a wider range of operating parameters.

3.2 Plasma Actuator Data

This section provides results and trends for using plasma actuators on the tail boom model and varying the actuator position, applied voltage and the flow velocity. To illustrate the effect of the plasma actuators on for a single test case, Figure 10 shows the pressure distribution when the actuators are off (black circles), when the actuators are on (red squares) and the estimated inviscid theoretical pressure distribution. The actuators are located at $(x/c)_a = 0.64$, the applied voltage is 11.7 kV_{p-p} and $Re = 7.3 \times 10^4$ ($U_\infty = 22.2$ ft/s, $(x/c)_s = 0.74$, $SD_{TB} = 0.10$). The pressure distribution for the actuator off case is similar to the baseline case shown in Figure 4 where the flow separates around $x/c = 0.65$. When the actuators are turned on, the pressure drops near the location of the actuators and the pressure in the separated flow region increases.

These changes in the pressure distribution are both beneficial for delaying flow separation and reducing pressure drag.

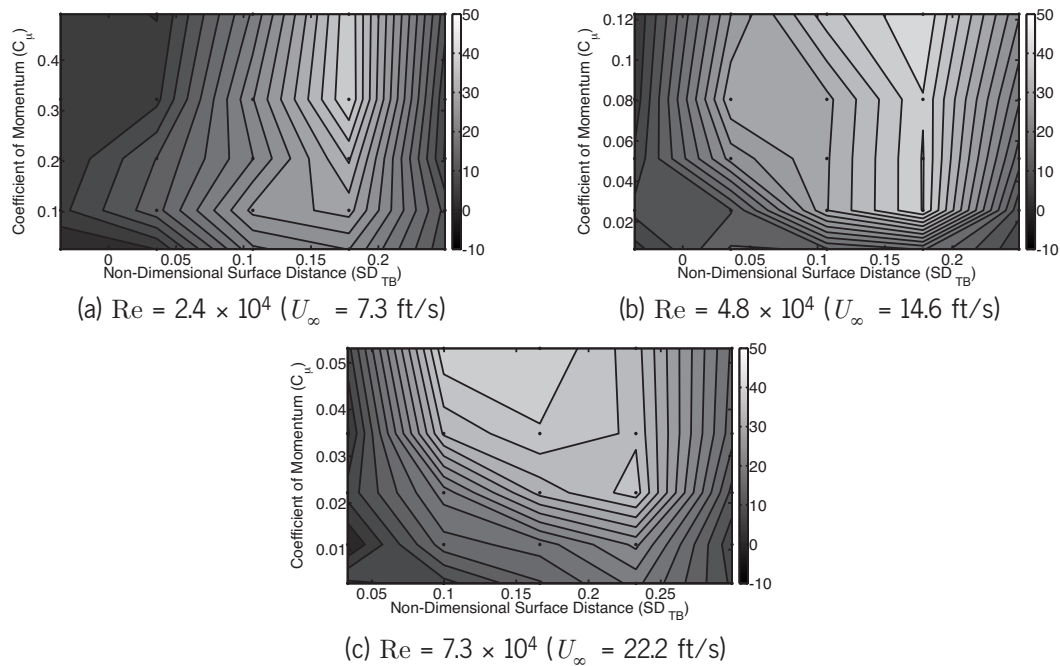


Figure 9. Non-dimensional surface distance (SD_{TB}) vs. applied voltage and the corresponding percentage of pressure drag reduction (color bar) for synthetic jet actuation.

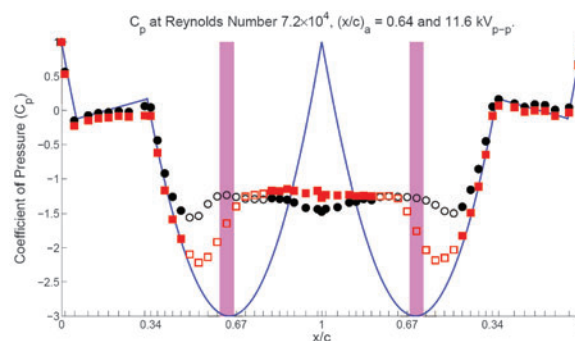


Figure 10. Pressure distribution showing the effect of two plasma actuators on the tail boom pressure distribution when placed at $(x/c)_a = 0.64$ with an applied voltage of 11.7 kV_{p-p} and $Re = 7.3 \times 10^4$. ($U_\infty = 22.2 \text{ ft/s}$, $(x/c)_s = 0.74$, $SD_{TB} = 0.10$)

3.2.1 Variation with Applied Voltage

Figure 11a shows the change in the pressure distribution as the applied voltage increases from 2.8 kV_{p-p} to 11.7 kV_{p-p} by increments of 1.4 kV_{p-p} . The actuators are located at $(x/c)_a = 0.64$ and $Re = 7.3 \times 10^4$ ($U_\infty = 22.2 \text{ ft/s}$, $(x/c)_s = 0.74$, $SD_{TB} = 0.10$). As the applied voltage increases, the pressure near the actuators decreases dramatically and the pressure in the separated flow region increases gradually. Also, the onset of flow separation moves downstream indicating that flow separation is delayed. All of these changes in the pressure distribution are beneficial for decreasing pressure drag.

Figure 11b shows the change in the percentage of pressure drag reduction as the applied voltage is increased. The percentage of pressure drag reduction is relatively constant up to 7 kV_{p-p} , beyond which, the pressure drag reduction increases until the applied voltage reaches 10 kV_{p-p} and then starts to level off. Increasing the applied voltage is similar to increasing C_μ and, as seen in previous sections where voltage is varied, there is a maximum attainable effectiveness when increasing C_μ has no additional benefit. The change in the pressure drag reduction at the highest applied voltages starts to show the same trend.

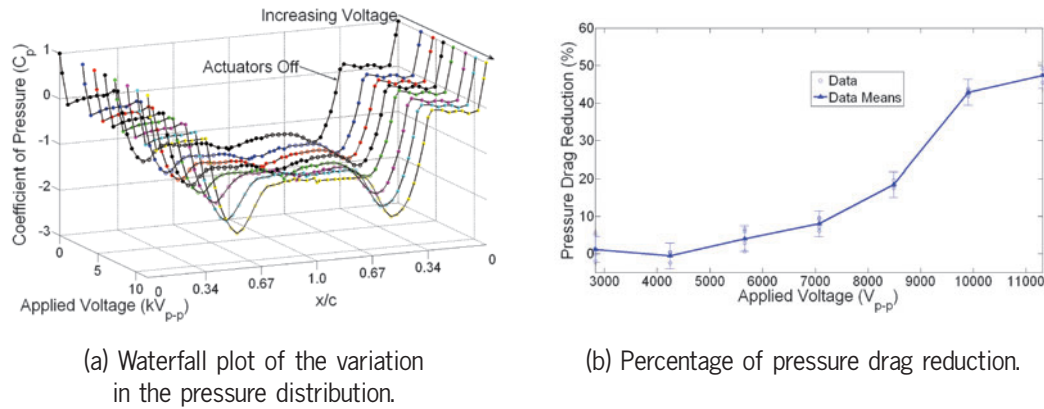


Figure 11. Variation as the applied voltage increases from 2.8 kV_{p-p} to 11.7 kV_{p-p} . ($Re = 7.3 \times 10^4$, $U_\infty = 22.2$ ft/s, $(x/c)_s = 0.74$, $(x/c)_a = 0.64$, $SD_{TB} = 0.10$)

3.3.2 Variation with Actuator Position

Figure 12a shows the variation in the pressure distribution as the actuator position moves downstream from $(x/c)_a = 0.43$ to 0.71. The applied voltage is 11.7 kV_{p-p} and $Re = 7.3 \times 10^4$ ($U_\infty = 22.2$ ft/s, $(x/c)_s = 0.74$). As the port location moves downstream, the pressure near the location of the actuators generally decreases until the actuators are at $(x/c)_a = 0.64$ but increases at $(x/c)_a = 0.71$. The pressure in the separated flow region also increases from $(x/c)_a = 0.64$ but decreases at $(x/c)_a = 0.71$.

At $(x/c)_a = 0.56$, there is evidence, based on the pressure distribution, of decreased effectiveness on one side ($x/c = 0$ to 1.0) and increased effectiveness on the other side ($x/c = 1.0$ to 0) of the model. This appears to be due to asymmetries in the actuator construction and placement. Because the drag coefficient is calculated based on the pressure distribution from $x/c = 0$ to 1.0, Figure 12b shows a decrease in actuator effectiveness at this point ($(x/c)_a = 0.56$). This also affected the polynomial fit of the mean line such that the values for $(x/c)_a = 0.49$ and 0.64 were excluded from the confidence interval. This point is not representative of the true trend and is believed to be higher than the value presented. Therefore, this point was not used in calculating the quadratic fit and the pressure drag reduction increases from $(x/c)_a = 0.49$ to 0.64 and decreases at $(x/c)_a = 0.71$. The peak in pressure drag reduction data corresponds to $SD_{TB} = 0.10$.

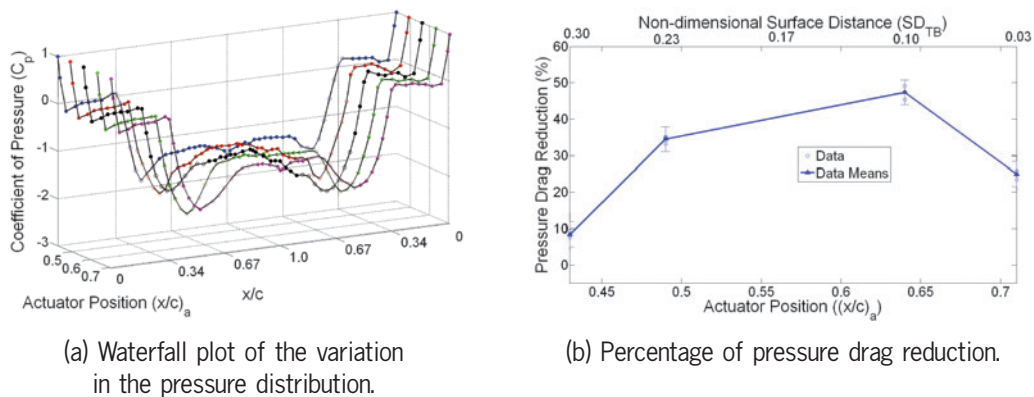


Figure 12. Variation as the actuator position moves downstream from $(x/c)_a = 0.43$ to 0.71. ($Re = 7.3 \times 10^4$, $U_\infty = 22.2$ ft/s, $(x/c)_s = 0.74$, $V = 11.7$ kV_{p-p})

3.3 SD_{TB} vs. Applied Voltage

As discussed in the previous sections, two factors influence the effectiveness of the actuators for reducing pressure drag: the applied voltage (similar to (C'_μ)) and the distance between the flow separation point and the actuator position (SD_{TB}). The following contour plots show the effect of both parameters on the percentage of pressure drag reduction for each velocity. The black points on the

contour plot represent the actual SD_{TB} and C_μ values for which the percentages of pressure drag reduction were taken.

Figure 13a shows the variation in pressure drag reduction as SD_{TB} and applied voltage for $Re = 2.4 \times 10^4$ ($U_\infty = 7.3$ ft/s). For constant applied voltage, there is relatively little change in the pressure drag reduction as SD_{TB} increases for applied voltages below 8 kV_{p-p}. For an applied voltage around 9 kV_{p-p}, the pressure drag reduction is largest at $SD_{TB} = 0.05$. For the highest applied voltage, the pressure drag reduction is largest for SD_{TB} greater than 0.15.

Figure 13b shows the variation in pressure drag reduction as SD_{TB} and applied voltage for $Re = 4.8 \times 10^4$ ($U_\infty = 14.6$ ft/s). For constant applied voltage, pressure drag reduction is fairly constant as SD_{TB} increases except at applied voltages above 8 kV_{p-p} where there is a peak in pressure drag reduction at $SD_{TB} = 0.05$. As the applied voltage increases above 8 kV_{p-p}, the peak pressure drag reduction occurs over a slightly wider range of SD_{TB} values. For a constant SD_{TB} , is fairly constant up to an applied voltage of 6 kV_{p-p}, beyond which, the pressure drag reduction quickly increases until the maximum effectiveness for that SD_{TB} value is achieved.

Figure 13c shows the variation in pressure drag reduction as SD_{TB} and applied voltage for $Re = 7.3 \times 10^4$ ($U_\infty = 22.2$ ft/s). For constant applied voltage, the pressure drag reduction is relatively constant as SD_{TB} increases for applied voltages below 8 kV_{p-p}. For applied voltages above 8 kV_{p-p}, pressure drag reduction increases quickly up to $SD_{TB} = 0.15$ and starts to decrease significantly past $SD_{TB} = 0.35$. However, there is a dip in the pressure drag reduction at $SD_{TB} = 0.25$.

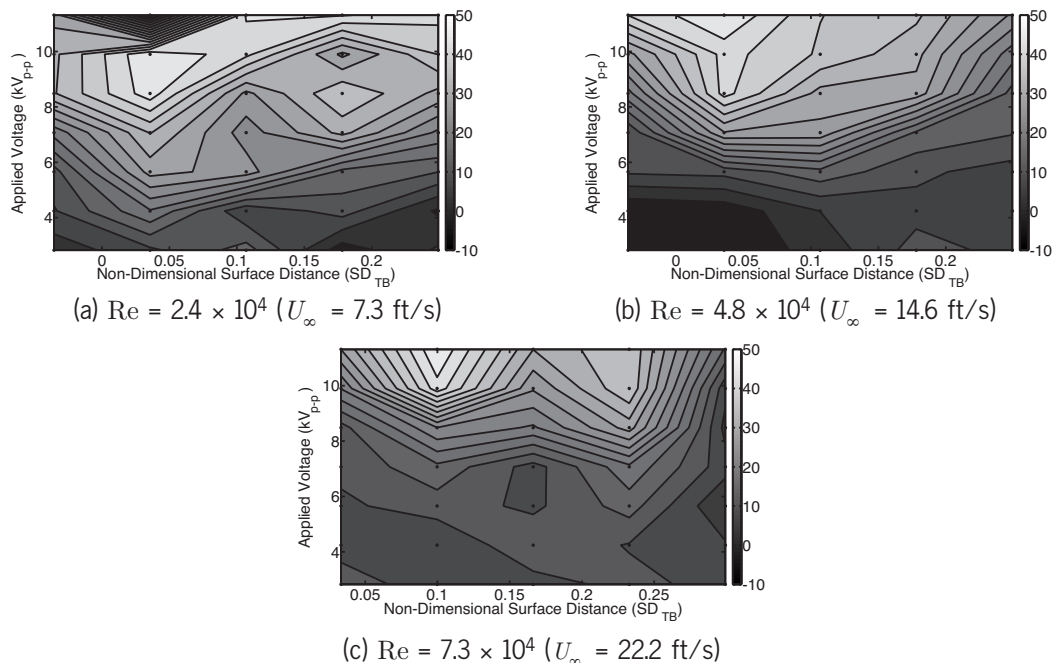


Figure 13. Non-dimensional surface distance (SD_{TB}) vs. applied voltage and the corresponding percentage of pressure drag reduction (color bar) for plasma actuation.

Based on all three plots (Figures 13a - 13c), the minimum applied voltage for significant pressure drag reduction increases as velocity increases which agrees with the trend of decreased actuator performance as C_μ decreases. There appears to be little connection in actuator performance between applied voltage and SD_{TB} values when looking at these three plots. Although never measured in this research, other research shows that C_μ is around $O(10^{-7})$ to $O(10^{-5})$ for plasma actuators and could support the decreasing range of actuator effectiveness as velocity increases. The high voltages used in the plasma actuators precluded use of a velocity sensor in close proximity to the devices, and thus values of C_μ were not available for the plasma actuators. It is expected that drag reduction associated with interaction between C_μ and SD_{TB} may have exhibited stronger correlation than voltage and SD_{TB} . In general, however, when the actuators are closer to the flow separation point, the maximum pressure drag reduction occurs at a lower applied voltage than when the actuators are farther from the flow

separation point. This trend is due to localized influence of the plasma actuators. When the actuators are close to the location corresponding to the minimum pressure coefficient, they have a large effect on $C_{p,min}$. When the actuators are closer to the rear half of the model, they affect the pressure in the separated flow region which has a slightly stronger influence on the total pressure drag reduction.

4. CONCLUSIONS

This paper shows the effect of varying applied voltage, Re and actuator position on the pressure distribution and the percentage of pressure drag reduction for each type of flow control device. In summary:

- 1) For synthetic jet actuation:
 - a) As voltage (C_μ) increases, the pressure distribution is increasingly influenced and the percentage of pressure drag reduction increases, especially beyond C_μ values above 0.2.
 - b) As the freestream velocity increases, the variation in the pressure distribution and percentage of pressure drag reduction do not follow the expected trend of decreasing effectiveness. Actuator effectiveness is actually dependant on the fixed location of the actuator relative to the changing location of flow separation (SD_{TB}) in addition to the momentum coefficient (C_μ).
 - c) As the actuator angular position moves downstream, the actuator effectiveness increases until a maximum is achieved based on the location of the actuator relative to the separation point.
 - d) There is an apparent optimal range for peak actuator performance between $SD_{TB} = 0.10$ and 0.25 , approximately.
- 2) For plasma actuation the same trends are seen as in the synthetic jet actuation except:
 - a) The minimum applied voltage required for significant pressure drag reduction increases with increasing velocity which matches the trend of decreased actuator performance as C_μ decreases.
 - b) The effect of the plasma actuators on the pressure distribution and pressure drag reduction depends on SD_{TB} . For relatively low values of SD_{TB} , the actuators affect the pressure in the separated flow region and result in higher pressure drag reduction results at lower applied voltages than for relatively high values of SD_{TB} .

Future work would involve an actual one-to-one comparison between these two devices. As mentioned in the body of this paper, the plasma actuator design would be altered to allow for higher applied voltages to match those produced by a synthetic jet actuator. Also, to further match operating conditions of the actuators, the synthetic jet orifice would be shaped such that the induced flow velocity would be tangent to the surface. Also, these devices have demonstrated the potential for significantly reducing pressure drag in low Reynolds number flows. Future research should also include a direct application of these devices on UAVs. To supply the power required for these devices, small, lightweight and efficient power supplies need to be developed, in addition.

ACKNOWLEDGMENTS

The author gratefully acknowledges Steve Wilkinson and the support of the NASA Langley Facility made possible through a Cooperative Research and Development Agreement with the Loads and Dynamics Division in the Vehicle Technology Directorate of the Army Research Laboratory at the Langley Research Center for helping with these experiments. Thanks to Dan Clingman at the Boeing Company for the synthetic jet actuator design and Dr. James Hubbard at the National Institute of Aerospace for providing amplifiers. The author also thanks the Boeing Company and the University of Maryland Minta Martin Aeronautical Research Fund Program for providing funds.

REFERENCES

1. Wilson, J. C. and Kelley, H. L., "Aerodynamic Characteristics of Several Current Helicopter Tail Boom Cross Sections Including the effect of Spoilers," *NASA Technical Paper 2506*, 1986, AVSCOM Technical Report 85-B-3.
2. Kelley, H. L., Crowell, C. A., Yenni, K. R., and Lance, M. B., "Flight Investigation of the effect of Tail Boom Strakes on Helicopter Directional Control," *NASA Technical Paper 3278*, 1993, AVSCOM Technical Report 93-A-003.

3. Sarioglu, M. and Yavuz, T., "Subcritical Flow Around bluff Bodies," *AIAA Journal*, Vol. 40, No. 7, July 2002, pp. 1257–1268.
4. Achenbach, E., "Distribution of local pressure and skin friction around a circular cylinder in cross-flow up to $Re = 5,000,000$," *Journal of Fluid Mechanics*, 1968.
5. Amitay, M., Honohan, A. M., Trautman, M., and Glezer, A., "Modification of the aerodynamic characteristics of bluff bodies using fluidic actuators," *AIAA Fluid Dynamics Conference*, 1997.
6. Glezer, A., Amitay, M., and Honohan, A. M., "Aspects of Low- and High-Frequency Actuation for Aerodynamic Flow Control," *AIAA Journal*, Vol. 43, No. 7, 2005.
7. Munska, M. D. and McLaughlin, T. E., "Circular Cylinder Flow Control Using Plasma Actuators," *43rd AIAA Aerospace Sciences Meeting and Exhibit*, 2005, AIAA Paper 2005-141.
8. McLaughlin, T. E., Felker, B., Avery, J. C., and Enloe, C. L., "Further Experiments in Cylinder Wake Modification with Dielectric Barrier Discharge Forcing," *44th AIAA Aerospace Sciences Meeting and Exhibit*, 2006, AIAA Paper 2006-1409.
9. Stepaniuk, V., Sheverev, V., Otugen, V., Tarau, C., Raman, G., and Soukhomlinov, V., "Sound Attenuation by Glow Discharge Plasma," *AIAA Journal*, Vol. 42, No. 3, 2004, pp. 545–550.
10. Zhuang, N., Alvi, F., Alkisar, M., and Shih, C., "Supersonic Cavity Flows and Their Control," *AIAA Journal*, Vol. 44, No. 1, 2006, pp. 2118–2128.
11. Sarpotdar, S., Raman, G., Sharma, S., and Cain, A., "Jet Impingement Tone Suppression Using Powered Resonance Tubes," *AIAA Journal*, Vol. 45, No. 5, 2007, pp. 972–979.
12. Glezer, A. and Amitay, M., "Synthetic Jets," *Annual Review of Fluid Mechanics*, Vol. 34, 2002.
13. Enloe, C. L., McLaughlin, T. E., Font, G. I., and Baughn, J. W., "Parameterization of Temporal Structure in the Single-Dielectric-Barrier Aerodynamic Plasma Actuator," *AIAA Journal*, 2006.
14. Enloe, C. L., McLaughlin, T. E., VanDyken, R. D., Kachner, K. D., Jumper, E. J., and Corke, T. C., "Mechanisms and Responses of a Single Dielectric Barrier Plasma Actuator," *41st AIAA Aerospace Sciences Meeting and Exhibit*, 2003, AIAA Paper 2003-1021.
15. Haack, S. J., *Flow Control Using Plasma and Synthetic Jet Actuators on bluff Bodies*, Master's thesis, University of Maryland, College Park, 2007.

